SUBMITTED TO AAS JOURNAL
Preprint typeset using LaTeX style emulateapj v. 12/16/11

SOLAR INTERNAL ROTATION INFERRED FROM HELIOSEISMIC DATA SPANNING MORE THAN TWO DECADES. I. INVERSION TECHNIQUES

MJT[1,2,3,4], ... JCD, ...

submitted to AAS journal

ABSTRACT

[SWSHO]

Subject headings: Sun: rotation — Sun: helioseismology — Sun: interior

1. INTRODUCTION

[Importance of solar rotation in various contexts, such as solar activity, solar evolution, as an example of general stellar rotation evolution.]

[Surface differential rotation. Roger?]

Already an early analysis of helioseismic data on high-degree modes by Deubner et al. (1979) showed the presence of a increase in the angular velocity with depth in the sub-photospheric layers. Analysis of sectoral modes by Duvall et al. (1984) demonstrated that the interior of the Sun rotates approximately as a solid body, wheras early data sensitive to the latitude variation of rotation showed the presence of a sharp gradient, the so-called *tachocline*, at the base of the convection zone (e.g., Christensen-Dalsgaard & Schou 1988; Brown et al. 1989; Dziembowski et al. 1989). Analysis of early results of the SOI/MDI instrument on the SoHO spacecraft (Schou et al. 1998) provided substantial details of solar internal rotation and the first **[??]** helioseismic evidence for subsurface zonal flows. Also, Eff-Darwich & Korzennik (2013) carried out a general analysis of rotation in the solar radiative interior.

Other investigations have focused on specific aspects of solar rotation. Charbonneau et al. (1999) and Antia & Basu (2011), amongst others, investigated the detailed properties of the tachocline. Zonal flows, and their relation to the solar magnetic activity cycle, have seen extensive investigations (e.g., Antia & Basu 2010; Vorontsov et al. 2002; Howe et al. 2000, 2009, 2018). Corbard & Thompson (2002) and Barekat et al. (2014) investigated the details of the near-surface shear in rotation. Finally, Chaplin et al. (1999) carried out an analysis aiming specifically at constraining rotation in the solar core.

Reviews of helioseismic investigations of solar internal rotation have been provided by, for example, Thompson et al. (1996, 2003) and Howe (2009).

Before the first helioseismic results it was generally assumed, based on simple arguments and early numerical simulations (e.g. Gilman 1976), that the solar convection zone showed 'rotation on cylinders', i.e., an angular velocity depending only on the distance to the rotation axis. The first analysis of the angular dependence of rotation within the convection zone showed this to be wrong, with rotation showing largely the same angular dependence as on the surface. This behaviour can to some extent be recovered by more complex hydrodynamical simulations of rotation and convection (e.g., Miesch et al. 2006). Given the likely rapid rotation of the Sun in the early phases of its evolution, angular momentum must have been lost, probably through a magnetically coupled solar wind (e.g., Kawaler 1988), directly affecting the convection zone. Thus the nearly uniform rotation in the radiative interior, and the formation of the narrow transition in the tachocline, requires efficient mechanisms for angular-momentum transport. This may involve magnetic fields (e.g., Gough & McIntyre 1998; Eggenberger et al. 2019) or wave transport (Talon & Charbonnel 2005), although the details are still far from clear.

[Brief overview (perhaps to be extended below) of facilities and data that are available (Jesper, Rachel, Rafa, Sylvain, ...?).]

Apart from the investigations, mentioned above, of the variation of solar rotation with the activity cycle, the extensive data accumulated by these facilities over the past two decades have seen relatively little use. Thus it is clearly time to make a comprehensive analysis to investigate the detailed properties of solar internal rotation and its possible variations with time, including an update of the available analysis techniques. With this in mind, Michael J. Thompson in 2017 established a wide-ranging collaboration to re-analyse and compare the available data, and carry out a full analysis of the resulting data. After Thompson's tragic early death in October 2019 the work has been carried out by the present group. **[I do find the previous two sentences appropriate, although we need to consider a possible conflict with making Michael first author of the paper.]**

[If separating into three(?) papers, need a few words on this here.]

[Briefly on the contents of the present paper.]

2. EFFECTS OF ROTATION ON STELLAR OSCILLATIONS

[One might consider, instead, having this material in an appendix, referred to in the observational section.]

The Sun is a slow rotator, and hence the effects of rotation on its oscillation frequencies can be determined from a perturbation analysis. To leading order in Ω (Hansen et al. 1977; Gough 1981; Brown et al. 1989)[1]

$$\delta\nu_{nlm} = \nu_{nlm} - \nu_{nl0} = \frac{m}{2\pi}\int_0^R \int_0^\pi K_{nlm}(r,\theta)\Omega(r,\theta) r \mathrm{d}r \mathrm{d}\theta \ , \quad (1)$$

where we neglected other possible departures from spherical symmetry, such as effects of magnetic fields. Here $\Omega(r,\theta)$ is the angular velocity, as a function of distance r to the centre and co-latitude θ, and R is the surface radius. Also, ν_{nlm} is

[1] **[For information, to be removed from the paper: Brown et al. (1989) give the first explicit expression for a general rotation law that I have found, although the other two papers implicitly have the general idea]**

jcd@phys.au.dk

the cyclic frequency of a mode characterized by radial order n, degree l and azimuthal order m, with $|m| \leq l$, and the *kernel* $K_{nlm}(r,\theta)$ is determined from the eigenfunction of the mode and the structure of the underlying solar model. It may be shown that the kernels depend only on $|m|$ and that they are symmetric around the equator:

$$K_{nl-m}(r,\theta) = K_{nlm}(r,\theta) \ , \quad K_{nlm}(r,\pi-\theta) = K_{nlm}(r,\theta) \ . \tag{2}$$

[Perhaps show a few examples of kernels.]

Rather than working in terms of the individual splittings $\delta\nu_{nlm}$ it is sometimes convenient to represent the dependence of the data on m in terms of the so-called a coefficients (see also Schou et al. 1998):

$$\delta\nu_{nlm} \approx \sum_{j=1}^{j_{\max}} a_j(n,l)\mathcal{P}_j^{(l)}(m) \ , \tag{3}$$

with, typically, $j_{\max} < 2l+1$; here the $\mathcal{P}_j^{(l)}$ are polynomials of degree j satisfying

$$\mathcal{P}_j^{(l)}(l) = l \ , \quad \sum_{m=-l}^{l} \mathcal{P}_i^{(l)}(m)\mathcal{P}_j^{(l)}(m) = 0 \quad \text{for } i \neq j \ . \tag{4}$$

It follows from Eqs (1) and (2) that rotation is represented by the coefficients a_j with odd j.

The a_j obtained from the fit in Eq. (3) to the splittings $\delta\nu_{nlm}$ are linearly related to the splittings. Thus it follows from Eq. (1) that $a_{2s+1}(n,l)$ is related to $\Omega(r,\theta)$ through an equation equivalent to Eq. (1), with a kernel $K^{(a)}_{nls}(r,\theta)$.

[I guess that we do not need to go into the use of expansions of Ω?]

3. OBSERVATION OF ROTATIONAL SPLITTINGS

[We need to consider the extent to which we shall make the data obtained and used generally available, and how. I strongly support an open data policy. The same of course goes for the results of the analyses.]

[The presentation of the data of course also needs error analysis.]

[Perhaps refer to Paper II for detailed analysis. Here we then just need enough to define the data set(s) used for the artificial data.]

4. HELIOSEISMIC INFERENCES OF SOLAR INTERNAL ROTATION

[The description below could deserve a few references for more detail.]

The goal of the analysis is to infer estimates $\overline{\Omega}(r_0,\theta_0)$ as a funtion of location (r_0,θ_0), as well as properties of the estimate, such as variance $\sigma^2(\overline{\Omega}(r_0,\theta_0))$ and the resolution of the inversion. This is based on the relation in Eq. (1) relating the observed splittings $\delta\nu_{nlm}$ to the true angular velocity, or the corresponding relations for the odd a coefficients $a_{2s+1}(n,l)$. For the observed quantities we need to take the errors in the observations into account. Thus we write Eq. (1) as

$$\Delta_k = \frac{2\pi}{m}\delta\nu_{nlm} = \int_0^R \int_0^\pi K_k(r,\theta)\Omega(r,\theta) r \mathrm{d}r\mathrm{d}\theta + \epsilon_k \ , \tag{5}$$

where $k \equiv (n,l,m)$, and ϵ_k corresponds to the error in the observations, with variance σ_k^2. Evidently there is a corresponding relation based on the a coefficients, with $k \equiv (n,l,s)$. Note that from the symmetry of the kernels around the equator, Eq. (2), it follows that the observations only provide information about the symmetric component of rotation, $\Omega^{(\mathrm{s})}(r,\theta) = 1/2[\Omega(r,\theta) + \Omega(r,\pi-\theta)]$.

In many cases the analysis involves linear operations on the observations. It follows that the inferred angular velocity at (r_0,θ_0) can be expressed as

$$\overline{\Omega}(r_0,\theta_0) = \sum_k c_k(r_0,\theta_0)\Delta_k \ , \tag{6}$$

in terms of *inversion coefficients* $c_k(r_0,\theta_0)$. From Eq. (5) we therefore obtain

$$\overline{\Omega}(r_0,\theta_0) = \int_0^R \int_0^\pi \mathcal{K}(r_0,\theta_0,r,\theta)\Omega(r,\theta) r \mathrm{d}r\mathrm{d}\theta + \epsilon(r_0,\theta_0) \ , \tag{7}$$

where

$$\mathcal{K}(r_0,\theta_0,r,\theta) = \sum_k c_k(r_0,\theta_0)K_k(r,\theta) \tag{8}$$

is the *averaging kernel*, normalized such that

$$\int_0^R \int_0^\pi \mathcal{K}(r_0,\theta_0,r,\theta)\mathrm{d}r\mathrm{d}\theta = 1 \ . \tag{9}$$

Also, $\epsilon(r_0,\theta_0)$ is the error in $\overline{\Omega}(r_0,\theta_0)$, with variance

$$\sigma^2(\overline{\Omega}(r_0,\theta_0)) = \sum_k c_k^2(r_0,\theta_0)\sigma_k^2 \ . \tag{10}$$

According to Eqs (7) and (9) the inferred angular velocity is an average of the true angular velocity weighted by $\mathcal{K}$. Thus the properties of $\mathcal{K}$ reflect the information contained in the inference. Typical examples of averaging kernels are shown in Fig. 1. As discussed in Section 4.4.1, the SOLA technique specifically designs the averaging kernel, in many cases resulting in a well-behaved kernel. On the other hand, in the RLSF technique the averaging kernel is to some extent a byproduct although, as shown, the inversion still provides a reasonably localized average of the angular velocity. Various measures, in addition to the target location, can be used to characterize location of the average, such as the location of the kernel maximum or the centre of gravity (CG). In the case of the RLSF the definition of the latter is complicated by the negative side lobes. **[This will need more detail for the individual techniques.]** Similar issues arise in the various measures that may be considered for the widths of the kernels in the radial and latitude directions. Perhaps the simplest measure is the full width at half maximum (FWHM), indicated in the figure.

We note that in these linear inversion methods the inversion coefficients do not depend on the data values Δ_k, only on the weights (typically determined by the standard deviations on the data) assigned to them, as well as obviously on the inversion technique and possible parameters characterizing the analysis. The same is therefore true of, for example, the averaging kernels. **[This seems obvious, but probably deserves a check.]**

[Descriptions of inversion techniques below need enough detail to define the parameters that are quoted.]

4.1. *Solar models and rotational kernels*

[This may need a few words. In particular, we might mention the uncertainties (or otherwise) associated with

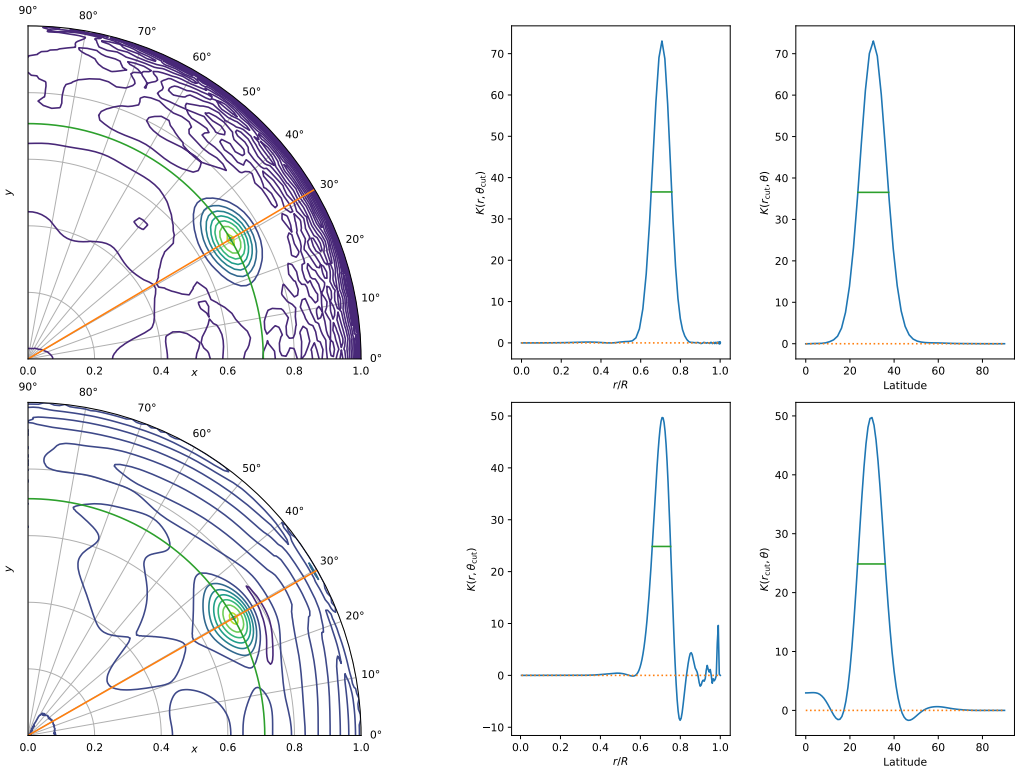

FIG. 1.— Averaging kernels for SOLA inversion at target location $(0.71R, 30.6°)$ (top; see Section 4.4.1) and RLSF inversion at $(0.70R, 30.0°)$ (bottom; see Section 4.3.1); the respective default inversion parameters were used. The left panels show contour plots of the kernels, the orange line and green circle **[colours, linestyles to be adjusted]** go through the maxima of the kernels, and the middle and right panels show cuts along these lines as functions of radius and latitude respectively; here the horizontal line marks the full width at half maximum.

the surface boundary condition and, more generally, with the known surface errors in the modelling.]

4.2. *1.5D inversion*

The expansion in Eq. (3) can be related directly to an expansion

$$\overline{\Omega}(r,\theta) = \sum_s \overline{\Omega}_s(r)\psi_s^{(1)}(x) \tag{11}$$

in suitable polynomials in $x = \cos\theta$, such that kernels $K^j_{nlj}(r)$ can be found, with

$$2\pi a_{2j+1}(n,l) = \int_0^R K^j_{nlj}(r)\overline{\Omega}_j(r)\mathrm{d}r \tag{12}$$

(Ritzwoller & Lavely 1991); a detailed analysis of these expansions was provided by Pijpers (1997). Equation (12) defines one-dimensional inverse problems for the expansion functions of $\overline{\Omega}$, which can be solved with the techniques discussed below. This inversion technique, often known as *1.5D inversion*, saw extensive use in early investigations of solar internal rotation. Schou et al. (1992) analysed its resolution properties and compared them with full 2D inversions, as considered here.

4.3. *Regularized least-squares fitting*

A commonly used technique is regularized least-squares fitting (RLSF), where a parametrized representation of $\overline{\Omega}$ is adjusted to match the observations. Since the fitting problem defined by Eq. (5) is ill-posed, with some kernels representing very similar measures of the angular velocity, the fitting has to be regularized. *Tikhonov regularization* (Tikhonov 1963) involves minimizing also the magnitude of the fit or variations in the fit. In helioseismology this is typically done by restricting rapidly varying components of the solution by suppressing its second derivative (see Eq. 14 below). Other types of regularization of the fit are discussed below.

In many cases $\overline{\Omega}$ is obtained implicitly through linear operations on the data (e.g., Christensen-Dalsgaard et al. 1990; Schou et al. 1994), which can be represented as in Eq. (6). It follows that in these cases the result of the inversion can be characterized by averaging kernels (Eq. 8).

[A little on the implementation, control of errors and resolution. A few examples of results, in particular averaging kernels suitably presented]

4.3.1. *The Antia and Basu implementation*

Here the odd-order splitting coefficients a_{2s+1} are analysed. This is done simultaneously in the latitudinal and radial directions. Details of the implementation are described by Antia et al. (1998). Briefly, the angular velocity $\overline{\Omega}$ is

represented by products of cubic B-splines in both radial and latitude directions, with 48 knots in r and 20 in θ. The knots in r are equidistant in acoustic radius

$$\tau = \int_0^r \frac{\mathrm{d}r}{c} \,, \tag{13}$$

where c is the adiabatic sound speed; the latitude behaviour is described as a function of $\cos\theta$, with knots that are equidistant in this quantity. The coefficients of the splines are determined by minimizing

$$\begin{aligned}
&\sum_k \sigma_k^{-2} \left[\Delta_k - \int_0^1 \mathrm{d}\hat{r} \int_{-1}^1 \mathrm{d}\cos\theta K_k(\hat{r},\theta)\overline{\Omega}(\hat{r},\theta) \right]^2 \\
&+\lambda_r \int_0^1 \mathrm{d}\hat{r} \int_{-1}^1 \mathrm{d}\cos\theta \hat{r}^{-1} \left(\frac{\partial^2\overline{\Omega}}{\partial\hat{r}^2} \right)^2 \\
&+\lambda_\theta \int_0^1 \mathrm{d}\hat{r} \int_{-1}^1 \mathrm{d}\cos\theta \sin^2\theta \left(\frac{\partial^2\overline{\Omega}}{\partial(\cos\theta)^2} \right)^2 \,,
\end{aligned} \tag{14}$$

where $\hat{r} = r/R$ is the dimensionless radius. The terms in the second derivatives of $\overline{\Omega}$ serve to regularize the solution, by suppressing rapid variations. The balance between this regularization and the fit to the observations is determined by the trade-off parameters λ_r and λ_θ. Increasing these parameters makes the solution smoother and in addition decreases the statistical error propagated from the observations (cf. Eq. 10), at the expense of making poorer the fit to the observations.

In the inversions reported here, default values of the parameters are $\lambda_r = 0.02$ and $\lambda_\theta = 0.1$.

[Check that the following still applies to the results shown: The smoothing parameters are selected to be the one that removes small-scale oscillations in the solution, while keeping the χ^2 of the fit reasonable. The uncertainty in the results are determined by boot-strapping; we have used 100 realizations of the data and inverted each set; the smoothing parameter was also changed randomly. The standard deviation of the 100 sets is our estimate of the error in the solution. Unlike the case of a simple error-propagation exercise, this allows us to take into account uncertainties caused by uncertainties in the smoothing parameter. The errors have been smoothed in (r, theta) by applying a running mean in two steps: first a running mean in 2d using 21 nearest points is used in the interior. After that a 15 point running mean only along radius is applied. The inversions are calculated on a grid with spacing of 2 degree in latitude and 0.005 Rsun in radius.]

4.3.2. *The Korzennik and Eff-Darwich implementation*

Inversion used Antonio Eff-Darwich's methods:

1 RLS/OMD (Eff-Darwich & Pérez Hernández (1997); files solution-m1_....) 2 Iterative Minimal Discrimination (Eff-Darwich et al. (2010); files solution-m2....)

Note that the inversion grid for the noisy data (aka err) is different from the noiseless case (aka noerr and flat) since the data are noisy and thus the spatial resolution is expected to be lower (the idea behind OMD: optimal mesh distribution).

The avg kernel width measure is

$$w^2 = 1/2 \int\int ((x - x_{acog})^2 + (y - y_{acog})^2)|K(x,y)|dxdy / \int\int |K(x,y)|dxdy \tag{15}$$

where acog is CoG of abs(kernel)

4.3.3. *Vorontsov implementation*

Technique which I use now is the same as before (see Vorontsov et al. 2002). It is iterative regularization with conjugate gradients in spectral domain (defined by expansion of the solution in 2D orthogonal polynomials with weight function defined by the prescribed data variances and sensitivity kernels). The cost function (or solution "merit") M is weighted rms mismatch with the data, i.e. when data errors are uncorrelated Gaussian (which we assume to be the case), the data is fitted at $M\sigma$ level. Regularization is achieved by terminating the iterative descents, based on simple visual inspection of the resulted solutions.

Iterative descents call for some initial guess to be provided. To speed up the convergence, it may be advantageous to use a few terms of 1.5D-inversion results (see Section 4.2). In the experiments reported below, we do not go that far, but implement a simple flat guess (uniform rotation) only. By its nature, gradient descents tend to provide the result close to the minimum-norm solution. For this reason, iteration started with some initial guess provides a solution which tends to be biased towards this particular guess. This property allows, by varying the initial guess, to address different solutions to the inverse problem which fit data at the same accuracy level, i.e. to address different members in the infinite family of solutions having the same likelihood. In its current implementation, my algorithm only works with data represented by the a_{2s+1} splitting coefficients.

4.4. *Optimally localized averages*

A different class of techniques for analysing helioseismic data are the *Optimally Localized Averages (OLA)* techniques, originally developed in geophysics (e.g., Backus & Gilbert 1968). Here the goal is to construct averaging kernels, by suitable choice of the inversion coefficients c_k to optimize the properties of the averaging kernel $\mathcal{K}$ (cf. Eq. 8). Although, in contrast to the RLSF techniques, this does not provide a direct fit to the observations the $\overline{\Omega}$ resulting from Eq. (6) does provide a good measure of the angular velocity according to Eq. (7) if $\mathcal{K}$ is suitably localized.

4.4.1. *Subtractive OLA*

The most common implementation of OLA in helioseismology is the so-called *subtractive* version, SOLA (Pijpers & Thompson 1992, 1994). Here the coefficients are determined such that $\mathcal{K}(\hat{r}_0,\theta_0,\hat{r},\theta)$ approximates a pre-defined *target function*, $\mathcal{T}(\hat{r}_0,\theta_0,\hat{r},\theta)$, by minimizing

$$\begin{aligned}
&\int_0^1 \int_0^{\pi/2} [\mathcal{T}(\hat{r}_0,\theta_0,\hat{r},\theta) - \mathcal{K}(\hat{r}_0,\theta_0,\hat{r},\theta)]^2 \hat{r}\mathrm{d}\hat{r}\mathrm{d}\theta \\
&\qquad +\mu^2 \sum_k c_k(\hat{r}_0,\theta_0)^2 \sigma_k^2 \,,
\end{aligned} \tag{16}$$

where for simplicity we assumed the observed splittings to be uncorrelated, and μ is a *trade-off parameter* controlling the magnitude of the variance of $\overline{\Omega}$ (cf. Eq. 10). **[Still need to check precise definition; see mail from RML, 16/11/20.]** In the implementation used here (Larsen 1998; Larsen & Hansen 1997; Larsen et al. 1998) Gaussian targets were used,

$$\mathcal{T}(\hat{r}_0,\theta_0,\hat{r},\theta) = A(\hat{r}_0,\theta_0) \exp\left[-\frac{(\hat{r}-\hat{r}_0)^2}{\Delta_r(\hat{r}_0)^2} - \frac{\hat{r}_0^2(\theta-\theta_0)^2}{\Delta_\theta^2} \right] \,, \tag{17}$$

where $A(\hat{r}_0,\theta_0)$ defines a suitable normalization. The width Δ_r in $\hat{r}$ scales with the adiabatic sound speed c,

$$\Delta_r(\hat{r}_0) = \Delta_{r,\mathrm{ref}} \frac{c(\hat{r}_0)}{c(\hat{r}_\mathrm{ref})} \ , \tag{18}$$

for a suitable reference radius $\hat{r}_\mathrm{ref}$; note also that Δ_θ defines the linear width in the latitude direction. The minimization problem defined by Eq. (16) leads to a set of linear equations for the coefficients c_k; efficient procedures for solving these equations were discussed by Larsen & Hansen (1997).

In the inversions reported here, default values of the parameters are $\Delta_{r,\mathrm{ref}} = 0.06$, $\Delta_\theta = 0.1$ and $\mu = 3.0$.

4.4.2. *Multiplicative OLA*

The original form of OLA is normally denoted *Multiplicative OLA* (MOLA) in the helioseismic community. There the coefficidents c_k are determined by minimizing

$$\int_0^1 \int_0^{\pi/2} [\mathcal{J}(\hat{r}_0,\theta_0,\hat{r},\theta)[\mathcal{K}(\hat{r}_0,\theta_0,\hat{r},\theta)]^2 \mathrm{d}\hat{r}\mathrm{d}\hat{r}\mathrm{d}\theta + \mu^2 \sum_k c_k(\hat{r}_0,\theta_0)^2 \sigma_k^2 \ , \tag{19}$$

where the weight function $\mathcal{J}$ is zero for $(\hat{r},\theta) = (\hat{r}_0,\theta_0)$ and rapidly increasing with distance from $(\hat{r}_0,\theta_0)$. Together with the normalization in Eq. (9) this ensures that $\mathcal{K}$ has the desired property of being large near $(\hat{r}_0,\theta_0)$ and suppressed elsewhere. This type of inversion was used by Chaplin et al. (1999) to investigate the rotation of the solar core. We do not consider it further here.

[Challenges of computational effort? Probably no longer relevant.]

4.5. *Validation of the inversion techniques*

To investigate the properties of the inversion techniques we have analysed artificial data computed for two angular-velocity profiles, illustrated in Fig. 2. One (Model 1) is based on an early analysis of data from the MDI instrument **[Rachel; did you make the analysis and can you identify where it may have been published?]** The second (Model 2) was set up analytically to include specific features, such as the tachocline and a 'jet' at high latitudes **[Sasha: perhaps it would be useful to quote the expressions used in an appendix.]** Given the angular velocity, splittings and splitting coefficients were computed for mode sets, including standard deviations that were obtained from solar data **[to be described, partly in Section 3]**. The analyses considered both the original splittings and splittings including Gaussian random errors, based on the observed standard deviations.

[A little on the dataset used for the test.]

[Describe metrics used to validate the analyses.]

As a measure of the region where the solution can be trusted we generally use the distance between the target location $(\hat{r}_0,\theta_0)$ and the location $(\hat{r}_\mathrm{CG},\theta_\mathrm{CG})$ of the centre of gravity

[Calculation of CG to be defined above, probably]:

$$\Delta_\mathrm{CG} = [(\hat{r}_\mathrm{CG}-\hat{r}_0)^2 + \hat{r}_0^2(\theta_\mathrm{CG}-\theta_0)^2]^{1/2} \ , \tag{20}$$

such that only the part of the inferred angular velocity for which $\Delta_\mathrm{CG} \leq \Delta_\mathrm{CG}^{(\mathrm{max})}$ is considered.

5. RESULTS

[Comparison of the properties of the RLSF and OLA techniques – advantages and disadvantages.]

[We probably need to present results for several independent analyses. This can be done in terms of the 'usual' plots (either 2D or lines at different latitudes or both). It would be good if one could distill results in numerical form that could be compared more quantitatively.]

Figure 3 shows results of applying the SOLA technique to Model 1. The left-hand panel, comparing the original and inferred rotation rate, clearly shows the smoothing of sharper features that is induced by the averaging kernel (cf. Eq. 8); this is particularly evident for the tachocline at latitude 60° and the 'jet' at latitude 75°. These features are also evident in the difference plot in the right-hand panel.

The dependence of the SOLA results on the parameters characterizing the inversion is illustrated in Fig. 5, in terms of root-mean-square averages of the difference between the inferred and original rotation rate and its standard deviation, the average taken over a region restricted by the difference between the target and centre-of-gravity locations. The left-hand column shows the decrease in standard deviation with increasing trade-off parameter μ, with a strong effect on $\langle\overline{\Omega}\rangle_\mathrm{rms}$ at higher latitude, whereas the effect is limited for latitude 45° and below. Increasing the widths of the target kernels substantially decreases the standard deviation and, in the case of $\Delta_{r,\mathrm{ref}}$, systematically increases $\langle\overline{\Omega}\rangle_\mathrm{rms}$. Interestingly, Δ_θ has little effect on $\langle\overline{\Omega}\rangle_\mathrm{rms}$ at low latitude, **[and the non-monotonic behaviour at 75° surely deserves further study.]**

[Perhaps some focus on results for the tachocline, including perhaps characterization of location and width.]

6. DISCUSSION

[This is perhaps where we discuss the properties of the solutions.]

[Advantages and disadvantages of different methods. Characterize them (here or above) also in terms of averaging kernels.]

[Ability to resolve the tachocline.]

7. CONCLUSIONS

[SWSHS]

Funding for the Stellar Astrophysics Centre is provided by The Danish National Research Foundation (Grant DNRF106).

REFERENCES

Antia, H. M., & Basu, S. 2010, ApJ, 720, 494, doi: 10.1088/0004-637X/720/1/494 1
—. 2011, ApJ, 735, L45, doi: 10.1088/2041-8205/735/2/L45 1
Antia, H. M., Basu, S., & Chitre, S. M. 1998, MNRAS, 298, 543, doi: 10.1046/j.1365-8711.1998.01635.x 4.3.1
Backus, G., & Gilbert, F. 1968, Geophysical Journal, 16, 169, doi: 10.1111/j.1365-246X.1968.tb00216.x 4.4
Barekat, A., Schou, J., & Gizon, L. 2014, A&A, 570, L12, doi: 10.1051/0004-6361/201424839 1
Brown, T. M., Christensen-Dalsgaard, J., Dziembowski, W. A., et al. 1989, ApJ, 343, 526, doi: 10.1086/167727 1, 2, 1

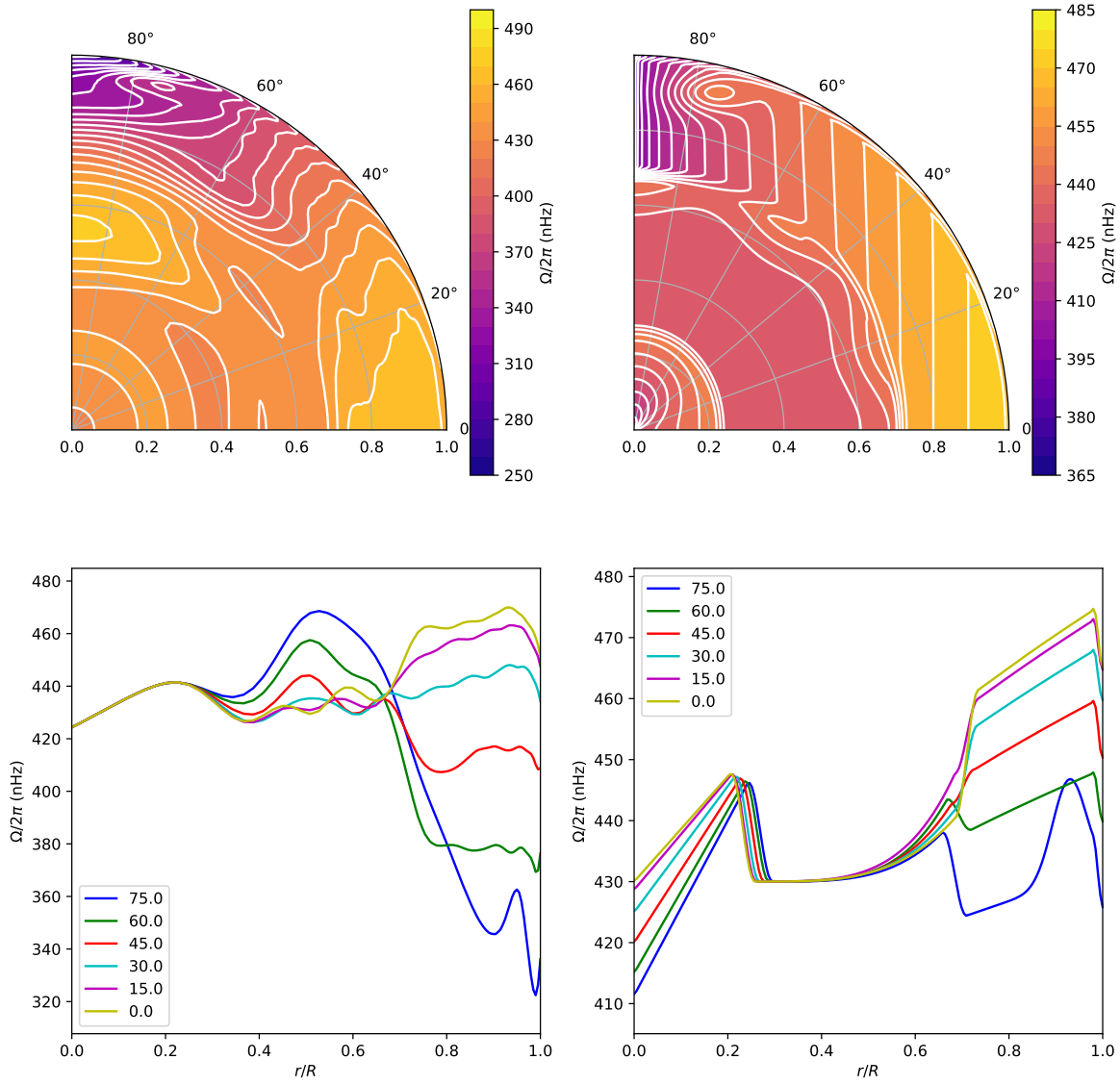

FIG. 2.— **[Artificial rotation profiles. Left: Model 1; right: Model 2.]**

Chaplin, W. J., Christensen-Dalsgaard, J., Elsworth, Y., et al. 1999, MNRAS, 308, 405, doi: 10.1046/j.1365-8711.1999.02691.x 1, 4.4.2

Charbonneau, P., Christensen-Dalsgaard, J., Henning, R., et al. 1999, ApJ, 527, 445, doi: 10.1086/308050 1

Christensen-Dalsgaard, J., & Schou, J. 1988, in ESA Special Publication, Vol. 286, Seismology of the Sun and Sun-Like Stars, ed. E. J. Rolfe, 149–153 1

Christensen-Dalsgaard, J., Schou, J., & Thompson, M. J. 1990, MNRAS, 242, 353, doi: 10.1093/mnras/242.3.353 4.3

Corbard, T., & Thompson, M. J. 2002, Sol. Phys., 205, 211, doi: 10.1023/A:1014224523374 1

Deubner, F.-L., Ulrich, R. K., & Rhodes, E. J., J. 1979, A&A, 72, 177 1

Duvall, T. L., J., Dziembowski, W. A., Goode, P. R., et al. 1984, Nature, 310, 22, doi: 10.1038/310022a0 1

Dziembowski, W. A., Goode, P. R., & Libbrecht, K. G. 1989, ApJ, 337, L53, doi: 10.1086/185377 1

Eff-Darwich, A., & Korzennik, S. G. 2013, Sol. Phys., 287, 43, doi: 10.1007/s11207-012-0048-z 1

Eff-Darwich, A., Korzennik, S. G., & García, R. A. 2010, Astronomische Nachrichten, 331, 890, doi: 10.1002/asna.201011420 4.3.2

Eff-Darwich, A., & Pérez Hernández, F. 1997, A&AS, 125, 391, doi: 10.1051/aas:1997229 4.3.2

Eggenberger, P., Buldgen, G., & Salmon, S. J. A. J. 2019, A&A, 626, L1, doi: 10.1051/0004-6361/201935509 1

Gilman, P. A. 1976, in Basic Mechanisms of Solar Activity, ed. V. Bumba & J. Kleczek, Vol. 71, 207 1

Gough, D. O. 1981, MNRAS, 196, 731, doi: 10.1093/mnras/196.3.731 2

Gough, D. O., & McIntyre, M. E. 1998, Nature, 394, 755, doi: 10.1038/29472 1

Hansen, C. J., Cox, J. P., & van Horn, H. M. 1977, ApJ, 217, 151, doi: 10.1086/155564 2

Howe, R. 2009, Living Reviews in Solar Physics, 6, 1, doi: 10.12942/lrsp-2009-1 1

Howe, R., Christensen-Dalsgaard, J., Hill, F., et al. 2009, ApJ, 701, L87, doi: 10.1088/0004-637X/701/2/L87 1

—. 2000, ApJ, 533, L163, doi: 10.1086/312623 1

Howe, R., Hill, F., Komm, R., et al. 2018, ApJ, 862, L5, doi: 10.3847/2041-8213/aad1ed 1

Kawaler, S. D. 1988, ApJ, 333, 236, doi: 10.1086/166740 1

Larsen, R. M. 1998, PhD thesis, Aarhus University 4.4.1

Larsen, R. M., Christensen-Dalsgaard, J., Kosovichev, A. G., & Schou, J. 1998, in ESA Special Publication, Vol. 418, Structure and Dynamics of the Interior of the Sun and Sun-like Stars, ed. S. Korzennik, 813 4.4.1

Larsen, R. M., & Hansen, P. C. 1997, A&AS, 121, 587, doi: 10.1051/aas:1997129 4.4.1, 4.4.1

Miesch, M. S., Brun, A. S., & Toomre, J. 2006, ApJ, 641, 618, doi: 10.1086/499621 1

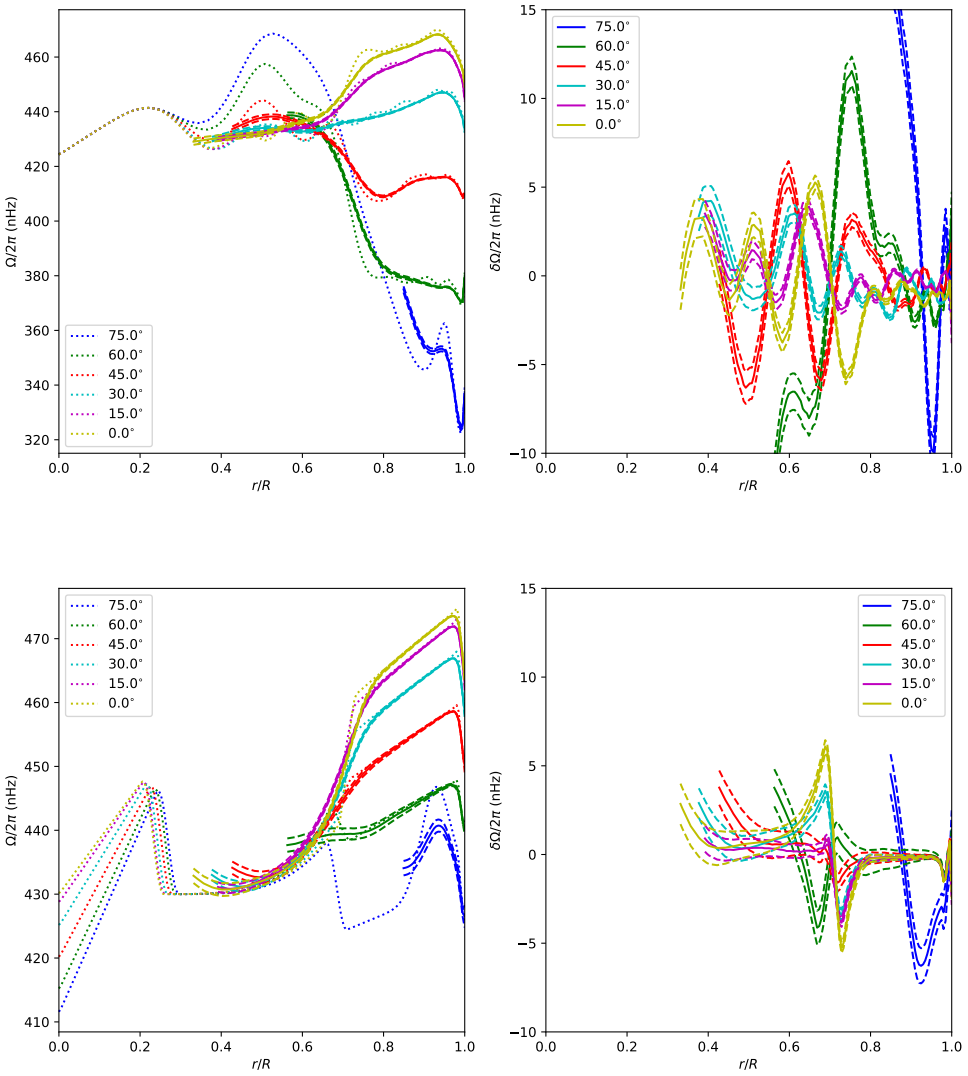

FIG. 3.— **[SOLA inversion, $\Delta_{r,\mathrm{ref}} = 0.06$, $\Delta_\theta = 0.1$, $\mu = 3$, against target radius, $\Delta_{\mathrm{CG}}^{(\max)} = 0.05$] [Top panel: Model 1, data sgk_model1_noerr_singlets-9-6400-hmi-32x. Bottom panel: Model 2, data sgk_model2_noerr_singlets-9-6400-hmi-32x.jsBo=0.2d]** In the left-hand panel the dotted lines show the rotation rate $\Omega_{\mathrm{mod}}/2\pi$ in the model and the solid lines show the inferred $\overline{\Omega}/2\pi$; the dashed lines show the inferred value $\pm\sigma(\overline{\Omega}/2\pi)$. The right-hand panel shows $\delta\overline{\Omega} = (\Omega_{\mathrm{mod}} - \overline{\Omega})/2\pi$, similarly indicating the standard deviation.

Pijpers, F. P. 1997, A&A, 326, 1235. https://arxiv.org/abs/astro-ph/9705234 4.2

Pijpers, F. P., & Thompson, M. J. 1992, A&A, 262, L33 4.4.1

—. 1994, A&A, 281, 231 4.4.1

Ritzwoller, M. H., & Lavely, E. M. 1991, ApJ, 369, 557, doi: 10.1086/169785 4.2

Schou, J., Christensen-Dalsgaard, J., & Thompson, M. J. 1992, ApJ, 385, L59, doi: 10.1086/186277 4.2

—. 1994, ApJ, 433, 389, doi: 10.1086/174653 4.3

Schou, J., Antia, H. M., Basu, S., et al. 1998, ApJ, 505, 390, doi: 10.1086/306146 1, 2

Talon, S., & Charbonnel, C. 2005, A&A, 440, 981, doi: 10.1051/0004-6361:20053020 1

Thompson, M. J., Christensen-Dalsgaard, J., Miesch, M. S., & Toomre, J. 2003, ARA&A, 41, 599, doi: 10.1146/annurev.astro.41.011802.094848 1

Thompson, M. J., Toomre, J., Anderson, E. R., et al. 1996, Science, 272, 1300, doi: 10.1126/science.272.5266.1300 1

Tikhonov, A. N. 1963, Soviet Math. Dokl., 4, 1035 4.3

Vorontsov, S. V., Christensen-Dalsgaard, J., Schou, J., Strakhov, V. N., & Thompson, M. J. 2002, Science, 296, 101, doi: 10.1126/science.1069190 1, 4.3.3

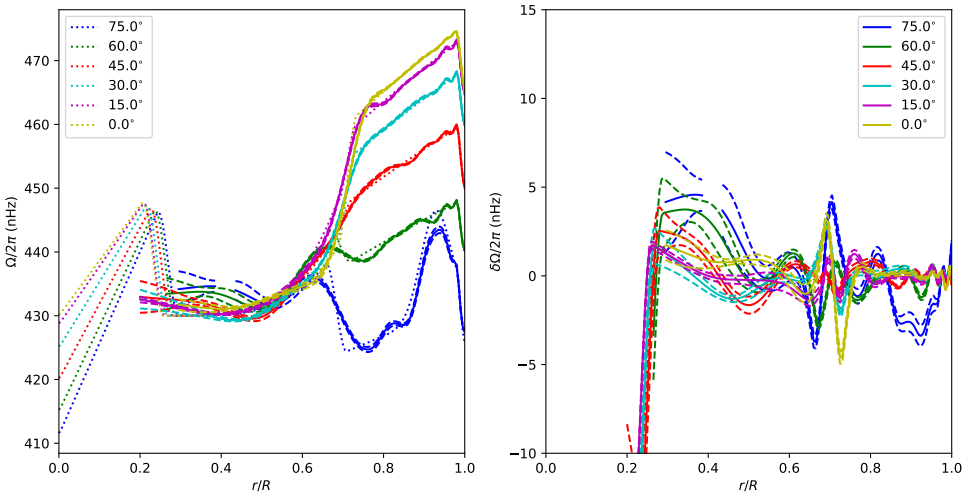

FIG. 4.— **[Results for Model 2, RLSF inversion (Antia and Basu), $\lambda_r = 0.02$, $\lambda_\theta = 0.1$, data js_model2_err_split10qr_191115.6400.36 against target radius, $\Delta_{\rm CG}^{(\rm max)} = 0.05$]** In the left-hand panel the dotted lines show the rotation rate $\Omega_{\rm mod}/2\pi$ in the model and the solid lines show the inferred $\overline{\Omega}/2\pi$; the dashed lines show the inferred value $\pm\sigma(\overline{\Omega}/2\pi)$. The right-hand panel shows $\delta\overline{\Omega} = (\Omega_{\rm mod} - \overline{\Omega})/2\pi$, similarly indicating the standard deviation.

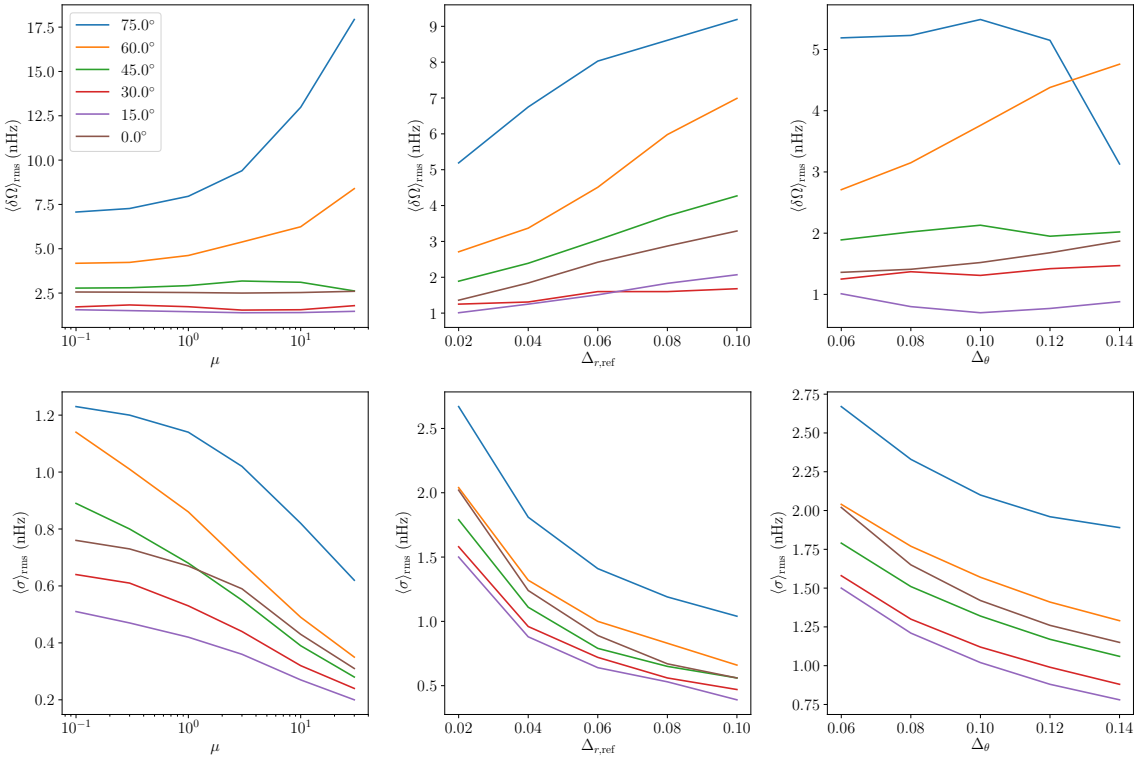

FIG. 5.— Dependence of SOLA inversions on the inversion parameters. The top row shows the root-mean-square difference between the inferred and model rotation rate, and the bottom row shows the rms standard deviation of the inference. In both cases, the mean is taken over the part of the solution where $\Delta_{\rm CG} \leq 0.05$ (cf. Fig. 3). The left column shows the dependence on the trade-off parameter μ, fixing parameters characterizing the target-kernel widths to $\Delta_{r,\rm ref} = 0.06$, $\Delta_\theta = 0.1$. The central column similarly shows the dependence on $\Delta_{r,\rm ref}$, for $\mu = 3$, $\Delta_\theta = 0.06$, and the right column shows the dependence on Δ_θ, for $\mu = 3$ and $\Delta_{r,\rm ref} = 0.02$. **[data from sgk_model1_noerr_singlets-9-6400-hmi-32x, no errors.]** **[Rachel: this is based on the set of inversions that you sent; I do not think that it includes the cases needed to use a fixed reference corresponding to the 'standard' set: $\Delta_{r,\rm ref} = 0.06, \Delta_\theta = 0.1, \mu = 3$?]**

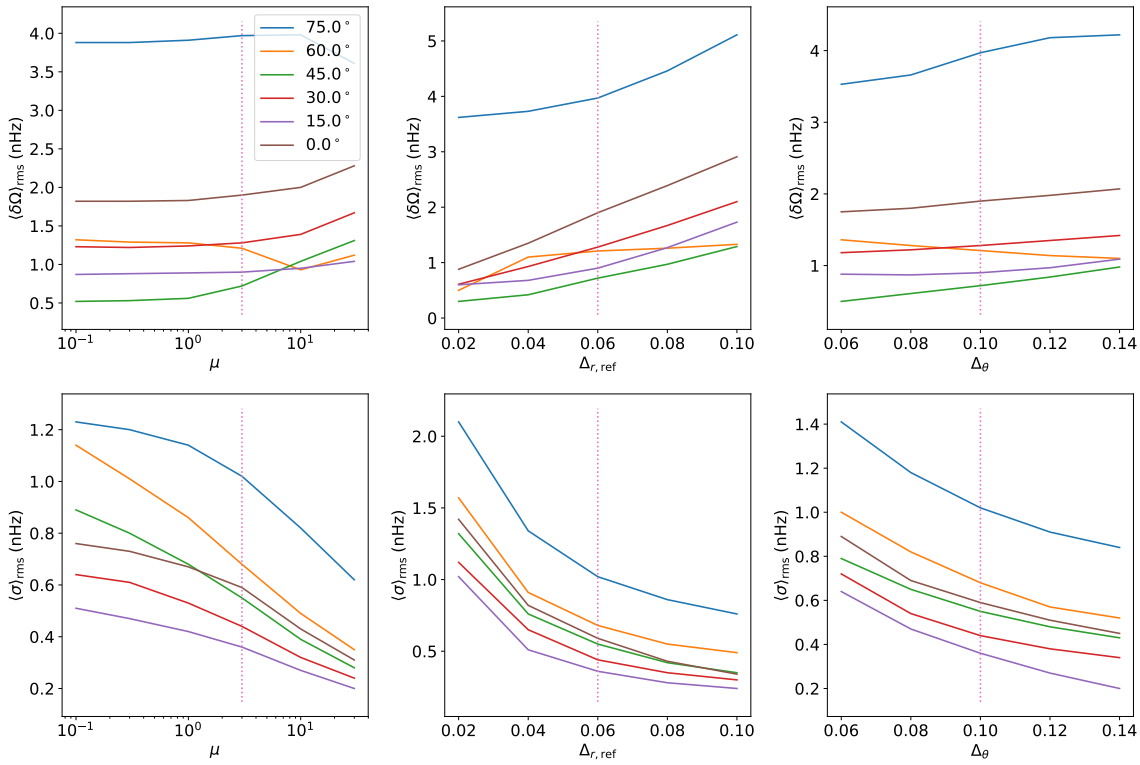

FIG. 6.— As Fig. 5, but for Model 2. Here the central column shows the dependence on $\Delta_{r,\mathrm{ref}}$, for $\mu = 3, \Delta_\theta = 0.1$, and the right column shows the dependence on Δ_θ, for $\mu = 3$ and $\Delta_{r,\mathrm{ref}} = 0.06$. In each column, the vertical dotted lines show the corresponding default values of the varying parameter. **[data from sgk_model2_noerr_singlets-9-6400-hmi-32x.jsBo=0.2d, no errors.]**